

Supplementary information for: "Near-field mechanism of the enhanced broadband magneto-optical activity of hybrid Au loaded Bi:YIG"

Spiridon D. Pappas,^{*a} Philipp Lang^a, Tobias Eul^a, Michael Hartelt^a, Antonio García-Martín^b, Burkard Hillebrands^a, Martin Aeschlimann^a, and Evangelos Th. Papaioannou^{*a,c}

Sample fabrication details

The samples used in our study were provided by Prof. Uchida's group in NIMS, Japan. The samples consist of Au nanoparticles (AuNPs), fabricated on top of a single crystalline GGG (111) substrate by post heating of a thin continuous Au film. On top of the AuNPs layer, a BiY₂Fe₅O₁₂ film is grown¹ by means of the metal-organic decomposition (MOD) method.² In this way, a hybrid Bi:YIG/AuNPs layer with a total thickness of 110 nm is produced on top of the GGG substrate, resulting to the final hybrid structure: BiY₂Fe₅O₁₂/AuNPs/GGG. The reference samples were fabricated by following the exact same procedure, without the AuNPs fabrication step though, resulting to the final structure: Pt/BiY₂Fe₅O₁₂/GGG.

Kerr rotation and ellipticity measurement example

The magnetic loops which are indicatively presented in Fig. 1(a), have been recorded in the L-MOKE geometry for the sample containing AuNPs. The rotation and ellipticity values have been extracted from each magnetic loop with the aid of the formula:

$$\theta_{s(p)} = \frac{\theta(H_{\text{ext}}^+) - \theta(H_{\text{ext}}^-)}{2} \quad (1)$$

where $H_{\text{ext}}^{+(-)}$ is an applied external field, sufficiently large to saturate the sample. The direction of the magnetic loop dictates the sign of the Kerr rotation value at each wavelength. Scanning from small to higher wavelength values, the amplitude of the magnetic loop becomes minimal at $\lambda = 650$ nm, and is subsequently inverted for higher wavelength values. Formula (1) was used similarly to extract the Kerr ellipticity values. In Fig. 1 (b), the extracted θ and ε spectra for the case of s-polarized incident light are indicatively presented.

Simulation technique

In our experimental MOKE setup, the laser source is located 1 m far from the sample position. This, implies that the incident electromagnetic wave on the sample, can be simulated by a plane wave, with a very good approximation. Therefore, the task is to simulate the optical/magneto-optical behavior of an infinitely extended film of gyrotropic material, when it is illuminated by a plane wave at an oblique angle of incidence. Numerical calculations were based on the Finite Integration Technique (FIT) method, by using the CST Microwave Studio (Computer Simulation Technology GmbH, Darmstadt, Germany).⁵ It is possible with CST to include in the calculations the off-diagonal elements of the dielectric tensor which are the responsible ones for the magneto-optical activity of the material. In order to simulate the optical properties of an infinitely extended Bi:YIG/GGG bilayer, without a huge computational effort on one hand, but without the possible edge effects introduced by the finite size of a bilayer slab on the other hand, we used "unit cell" boundary conditions. Unit cell boundary conditions allow to apply Floquet-Bloch periodic boundary conditions on the boundaries of a basic cell (unit cell):

$$\mathbf{E}(x + m\Lambda_x, y + n\Lambda_y, t) = \mathbf{E}(x, y, t)e^{ik_x m\Lambda_x} e^{ik_y n\Lambda_y} e^{-it} \quad (2)$$

where E is the electric field vector, Λ_x and Λ_y are the periodicities along x and y directions correspondingly, k_x and k_y are the wavevector components of E on the x and y directions, and m, n are integers denoting the number of the cell. In this way, the proper boundary conditions are calculated by the package for an oblique angle of incident light, and the behavior of an infinitely extended layer can be visualized. It is worth to notice at this point, that the introduction of periodicity for the simulated Bi:YIG/AuNPs/GGG structure has very minor spurious effects. This is explained by the fact that the nanoparticles are sufficiently far apart from each other, and therefore there is no (or very little) interaction between them. The latter was also verified by running a series of simulations with different edge-to-edge distances between the particles. The obtained differences in the far-field spectra were actually very small, meaning that the nature of the simulated resonances is localized rather than propagating. On the other hand, the usage of Floquet periodic boundary con-

^a Department of Physics and Research Center OPTIMAS, University of Kaiserslautern, 67663 Kaiserslautern, Germany. E-mail: pappas@rhrk.uni-kl.de

^b Instituto de Micro y Nanotecnología IMN-CNM, CSIC, CEI UAM+CSIC, Isaac Newton 8, E-28760 Tres Cantos, Madrid, Spain.

^c Institute of Physics, Martin-Luther University Halle-Wittenberg, Von-Danckelmann-Platz 3, 06120 Halle, Germany. E-mail: evangelos.papaioannou@physik.uni-halle.de

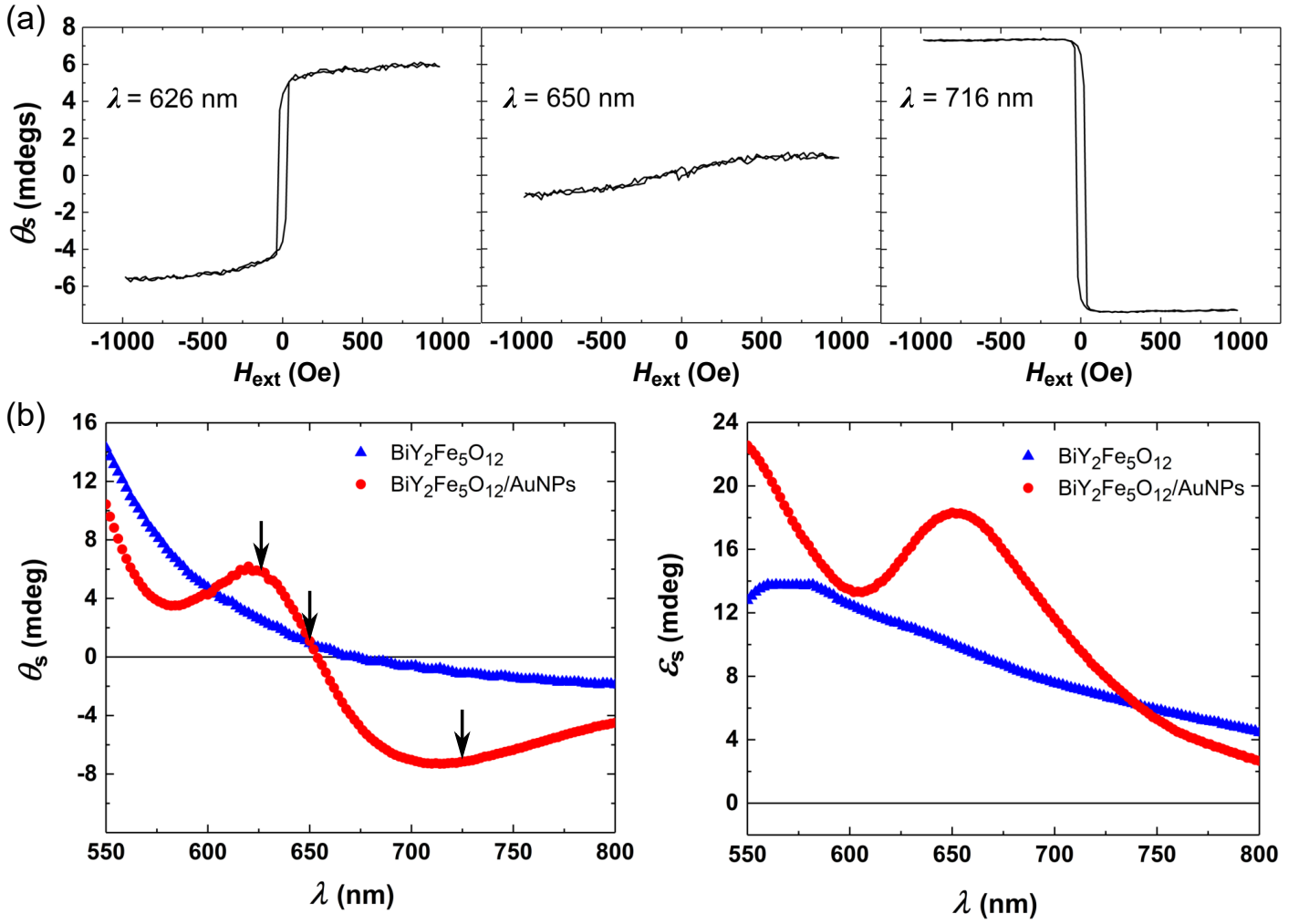


Fig. 1 (a) Magnetic loops recorded in the longitudinal MOKE geometry for the $\text{BiY}_2\text{Fe}_5\text{O}_{12}/\text{AuNPs}$ sample, at three different wavelength values. (b) Plots of Kerr rotation (θ_s) and ellipticity (ϵ_s) for s-polarized incident light, as a function of wavelength. The experimental points which are indicated with arrows in the θ_s versus λ plot, have been obtained from the corresponding magnetic loops which are shown in (a).

ditions help to avoid edge effects in the far-field arising from the edges / discontinuity of the Bi:YIG material. By using the unit cell periodic boundary conditions we effectively simulate a continuous Bi:YIG film which incorporates Au inclusions, where the periodicity of the inclusions has been confirmed to introduce no (or very minor) spurious effects. The “unit-cell” boundary conditions option can be used with the “frequency domain solver”. The simulated structure in this case is excited by a single-frequency plane wave and the simulation is performed at the steady state. The simulated structure was meshed by using a tetrahedral grid, with the option “adaptive refinement” enabled. Tetrahedrons are the simplest volume entities used in 3-D EM field simulation packages, since they offer great flexibility in approximating arbitrary geometries.^{6,7} Adaptive refinement, ensures that all the details of the simulated geometry are meshed adequately. In the frequency domain, only a single frequency point is simulated in every run. The broadband behavior of the structure is obtained by simulating multiple frequency points. The magneto-optical Kerr effect, which refers to this change of the polarization state of the reflected light, can be described phenomenologically with the aid

of the reflectivity matrix:

$$S_R = \begin{pmatrix} r_{ss} & r_{sp} \\ r_{ps} & r_{pp} \end{pmatrix} \quad (3)$$

where the elements r_{xy} are the Fresnel coefficients. S_R relates the state of the incident light with the state of the reflected light as follows:

$$\begin{pmatrix} E_s^r \\ E_p^r \end{pmatrix} = \begin{pmatrix} r_{ss} & r_{sp} \\ r_{ps} & r_{pp} \end{pmatrix} \begin{pmatrix} E_s^i \\ E_p^i \end{pmatrix} \quad (4)$$

where the subscripts s and p denote s- and p- polarized light, respectively. By properly defining Floquet ports we can represent the optical system as a port network using an analogy from the circuit theory. In this way, the S-matrix of the system can be calculated, which provides the ratio of the reflected electric field over the incident electric field. Therefore, the r_{ss} , r_{pp} , as well as the r_{sp} and r_{ps} elements can be calculated in this way. A Floquet port behaves like a wave port, in the sense that the electric field on the boundary of the port is represented by a summary of modes (Floquet modes). As a wave port, it allows the injection of a

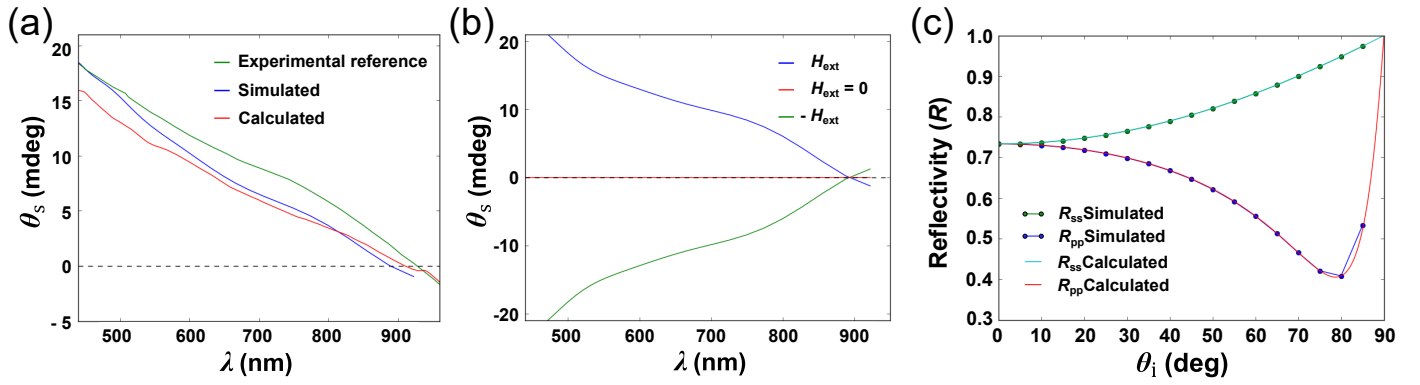


Fig. 2 (a) Kerr rotation as a function of wavelength for continuous Ni films simulated with the aid of CST (blue line) and analytically calculated (red line). The diagonal and off-diagonal elements of the dielectric tensor was used from the literature^{3,4} for both cases. The green line corresponds to the experimental data obtained for a continuous Ni film which was used as a calibration sample. (b) Simulated Kerr rotation curves for a continuous Ni film as a function of wavelength, for externally applied magnetic fields of different signs (blue and green curves), as well as for the case of no external field applied. (c) Simulated and calculated R_{ss} and R_{pp} for a continuous film for different angles of incidence.

plane wave (e.g. incident light) or the detection of the reflected or transmitted electric field. A Floquet port allows for modal decomposition of the electric field on its boundary, and therefore it is the basic tool to analyze periodic metasurfaces. In these structures, the reflection and transmission can be seen as the interference of an infinite number of propagating and evanescent waves (Floquet modes). With the Floquet ports, it becomes feasible to calculate the elements of the S-matrix which interconnect all the combinations of the different modes presented. In our studies, only the basic Floquet harmonic ($n=0$) is examined which should be the main component of the reflected light in the specular geometry. The accuracy of the simulated magneto-optical response for the Bi:YIG structures, obtained with the aid of the CST package, was tested *a priori* through a series of verification simulations for the case of a continuous Ni film. The dielectric tensor of Ni was derived from the literature.^{3,4} The Fresnel coefficients r_{ss} , as well as the polarization conversion coefficients r_{ps} for the case of longitudinal MOKE (LMOKE) were calculated analytically and the resulting Kerr rotation was compared with the simulated ones provided by the CST package. The results of the verification tests are presented in Fig. 2.(a-c). Starting from Fig. 2(c), we see the excellent matching between the analytically calculated and the simulated reflectivity for s- and p-polarized light. In Fig. 2(a) the simulated and analytically calculated Kerr rotation is presented (blue and red lines correspondingly). It can be observed that the results are matching very well and the small difference between them is mainly attributed to the fitting functions of the dielectric tensor values. In the same plot, the data of an L-MOKE measurement of a continuous Ni film is presented (green line) as reference. In Fig. 2(b) the simulated Kerr rotation curves for a continuous Ni film, for externally applied magnetic fields of different signs (blue and green curves), as well as for the case of no external magnetic field, are shown. The inverted sign is simulated by inverting the sign of the off-diagonal elements of the dielectric tensor.

Physical meaning and derivation of Eqs. 6 and 7

In order to get physical insight on the rigorous CST numerical results, and thus on the experimental evidences, we present in Eqs. 6 and 7 of the main text, the diagonal and off-diagonal elements of the electric polarizability for small (Rayleigh limit) dipolar particles. This limit considers that the field inside the particle is constant, and therefore it can be written as:⁸⁻¹¹

$$\overleftrightarrow{\alpha} = (\overleftrightarrow{\alpha}_0 - i \frac{k^3}{6\pi} \overleftrightarrow{T})^{-1} \quad (5)$$

$$\overleftrightarrow{\alpha}_0 = (\overleftrightarrow{\epsilon}^P - \overleftrightarrow{\epsilon}^{\text{Env}})(\overleftrightarrow{\epsilon}^P - \overleftrightarrow{\epsilon}^{\text{Env}} + \overleftrightarrow{L}^{-1} \overleftrightarrow{\epsilon}^{\text{Env}})^{-1} \overleftrightarrow{L}^{-1} V \quad (6)$$

where $\overleftrightarrow{\alpha}_0$ is the 3x3 electrostatic polarizability tensor, $i \frac{k^3}{6\pi} \overleftrightarrow{T}$ stands for the radiative corrections, \overleftrightarrow{T} is the unit 3x3 dyadic, $\overleftrightarrow{\epsilon}^P$ is the 3x3 dielectric tensor of the particle, $\overleftrightarrow{\epsilon}^{\text{Env}}$ is the 3x3 dielectric tensor of the environment, \overleftrightarrow{L} is the 3x3 depolarization tensor accounting for shape anisotropies (diagonal where $L_{xx} + L_{yy} + L_{zz} = 1$) and V is the volume of the particle. In $\overleftrightarrow{\alpha}_0$ the wavelength dependence (dispersion) is only arising from that of $\overleftrightarrow{\epsilon}^P$ and $\overleftrightarrow{\epsilon}^{\text{Env}}$. It is worth noticing that both $\overleftrightarrow{\epsilon}^P$ and $\overleftrightarrow{\epsilon}^{\text{Env}}$ can be non-diagonal and present magneto-optical activity. Also, for absorptive systems and particles whose radius is notably smaller than the wavelength of the impinging light, we can consider that $\overleftrightarrow{\alpha} \approx \overleftrightarrow{\alpha}_0$. From Eq. 6 it is readily apparent that the particle polarizability exhibits polarization conversion that can be originated either from the material that the particle is made of or from its coupling to the environment, or from both. In order to give insight on our particular case, we have to use the very same conditions used in the CST calculations. Here, we should notice that:

- $\overleftrightarrow{\epsilon}^P = \overleftrightarrow{\epsilon}^{\text{Au}}$ is a diagonal 3x3 matrix with all elements equal. The small inherent magneto-optical activity of AuNPs is neglected here, as this would have negligible effect on our calculations.
- $\overleftrightarrow{\epsilon}^{\text{Env}} = \overleftrightarrow{\epsilon}^{\text{Bi:YIG}}$ is a 3x3 matrix where the diagonal is equal for all elements and there are two non-zero off diagonal elements $\epsilon_{yz} = -\epsilon_{zy}$.

- L is in this case $L_{xx} = L_{yy} \neq L_{zz}$ and $L_{xx} + L_{yy} + L_{zz} = 1$, accounting for the oblate anisotropy (aspect ratio) of the particles.

With the above definitions and keeping the linear response it is straightforward to derive Eqs. 6 and 7 in the main text.

Notes and references

- 1 H. Uchida, Y. Masuda, R. Fujikawa, A. V. Baryshev and M. Inoue, *J. Magn. Magn. Mater.*, 2009, **7**, 843.
- 2 K. Uchida, H. Adachi, D. Kikuchi, S. Ito, Z. Qiu, S. Maekawa and E. Saitoh, *Nature Communications*, 2015, **6**, 5910.
- 3 P. B. Johnson and R. W. Christy, *Phys. Rev. B*, 1974, **9**, 5056.
- 4 T. Yoshino and S.-I. Tanaka, *Optics Communications*, 1969, **1**, 149.
- 5 *CST - Computer Simulation Technology*, CST.
- 6 T. Weiland, M. Timm and I. Munteanu, *IEEE Microwave Magazine*, 2008, **9**, 62.
- 7 *CST Microwave Studio 2017, Workflow and Solver Overview*, CST - Computer Simulation Technology AG, 2017.
- 8 D. Bedeaux and P. Mazur, *Physica*, 1973, **67**, 23.
- 9 V. V. Varadan, A. Lakhtakia and V. K. Varadan, *IEEE Transactions on Antennas and Propagation*, 1989, **37**, 800.
- 10 S. Albaladejo, R. Gómez-Medina, L. S. Froufe-Pérez, H. Marinchio, R. Carminati, J. F. Torrado, G. Armelles, A. García-Martín and J. J. Sáenz, *Opt. Express*, 2010, **18**, 3556.
- 11 N. de Sousa, L. S. Froufe-Pérez, J. J. Sáenz and A. García-Martín, *Sci. Rep.*, 2016, **6**, 30803.